A APPENDIX

In the Appendix section, we provide more detailed description to our model, more experiment results, as well as additional remarks.

A.1 BLOCH EQUATIONS

The Bloch equations based MR physics governs signal formation, which involves spin dynamics, quantum mechanics and electromagnetism. They are composed of a set of linear ordinary differential equations in matrix form:

$$\frac{dM}{dt} = \begin{bmatrix} -1/T2 & \gamma B_z & -rB_y \\ -\gamma B_z & -1/T2 & \gamma B_x \\ \gamma B_y & -\gamma B_x & -1/T1 \end{bmatrix} M + \begin{bmatrix} 0 \\ 0 \\ M_0/T1 \end{bmatrix}$$

where $M = \begin{bmatrix} M_x \\ M_y \\ M_z \end{bmatrix}$. The Bloch equations represent a nonlinear mapping from per-voxel intrinsic tissue properties to the corresponding temporal signal evolution. It describes discrete spin motion at small time interval that records the magnetisation response of proton dipoles to dynamic excitations induced by the RF sequence. The dynamics process can be characterized by 3 stages: nutation and forced precession caused by RF pulse, rotation caused by gradient magnetic field, and relaxation after removing RF pulse. Thus, this dynamic process can be described with successive operators according to a specific MR pulse sequence.

RF effect. Each RF pulse excitation applies a rotation on the magnetization M as:

$$M' = R_{\theta,\phi} M$$

where $R_{\theta,\phi}$ denotes the rotation caused by RF with arbitrary B_1 direction. It is formulated as

$$R_{\theta,\phi} = R_z(-\phi) R_y(-\theta) R_z(\alpha) R_y(\theta) R_z(\phi)$$

where $\phi = \tan^{-1}(B_y/B_x)$, $\theta = \tan^{-1}(|B_{xy}/B_z|)$

For instance, the RF pulse with flip angle α leads to a rotation on M along x, y axis:

$$M' = R_x(\alpha) M = \begin{bmatrix} 1 & 0 & 0 \\ 0 & \cos\alpha & \sin\alpha \\ 0 & -\sin\alpha & \cos\alpha \end{bmatrix} M$$

and

$$M' = R_y(\alpha) M = \begin{bmatrix} \cos\alpha & -\sin\alpha & \\ 0 & 1 & 0 \\ \sin\alpha & 0 & \cos\alpha \end{bmatrix} M$$

Gradient effect. The gradient / ΔB_0 causes rotation of angle θ on M along z axis:

$$M' = R_z(\theta) M = \begin{bmatrix} \cos\theta & \sin\theta & 0 \\ -\sin\theta & \cos\theta & 0 \\ 0 & 0 & 1 \end{bmatrix} M$$

where $\theta = \gamma(G \cdot \vec{r} + \Delta B_0)\tau$

Relaxation effect. The relaxation over time period τ gives:

$$M' = \begin{bmatrix} E_2 & 0 & 0 \\ 0 & E_2 & 0 \\ 0 & 0 & E_1 \end{bmatrix} M + \begin{bmatrix} 0 \\ 0 \\ M_0(1 - E_1) \end{bmatrix}$$

where $E_1 = \exp(-\tau/T1)$, and $E_2 = \exp(-\tau/T2)$

The rotations and relaxations can be combined and then propagated along L time points, leading to:

$$M_1 = A_1 M_0 + B_1; M_2 = A_2 M_1 + B_2; \ldots; M_L = A_L M_{L-1} + B_L$$

which is equivalent to:

$$M_L = AM_0 + B$$

where $A = \prod_{i=L}^{1} A_i$ and $B = \sum_{i=1}^{L} \left(\prod_{j=L}^{i+1} A_j\right) B_i = \left(\prod_{i=L}^{2} A_i\right) B_1 + \ldots + A_L B_{L-1} + B_L$

The differentiability of Bloch equations. Under some conditions, typically simple RF sequences and with assumed steady-state, there exist analytic (closed-form) solutions, e.g. $M = M_0(1 - \exp(-TR/T1))\exp(-TE/T2)$ for spin-echo pulse sequence. Then, it is apparent that M is differentiable with respect to tissue properties T1, and T2. However, for a complex pulse sequence, analytical solutions are hard to obtain due to spin history effects at unsteady-states and system imperfections. For example, in MR fingerprinting, various sequence components are varied in a pseudo-random pattern. In such cases, the solutions are also numerically differentiable with respect to T1, T2.

A.2 EPG FORMALIZATION

Extended phase graphs (EPG) is a popular and powerful formalism to solve Bloch equations in the Fourier domain. It provides fast and precise quantitation of echo intensities by characterizing the effect of gradients, radio frequency (RF) pulses and relaxation during the MR sequence as the action of a few matrix operations on the configuration states, a.k.a. phase states [59], a key concept based on the Fourier decomposition of transverse magnetization.

Define a new transverse magnetization M_{xy} as the combination of M_x and M_y:

$$M_{xy} = M_x + iM_y$$

This leads to a new matrix form for the magnetization with the following relation to the previous one:

$$\begin{bmatrix} M_{xy} \\ M_{xy}^* \\ M_z \end{bmatrix} = \begin{bmatrix} 1 & i & 0 \\ 1 & -i & 0 \\ 0 & 0 & 1 \end{bmatrix} \begin{bmatrix} M_x \\ M_y \\ M_z \end{bmatrix}$$

The Fourier coefficients F_n^+, F_n^-, Z_n of the magnetization lead to the configuration state matrix Q as:

$$F_n^+ = \int_0^1 M_{xy}(z) e^{-2\pi i n z} dz$$

$$F_n^- = F_{-n}^* = \int_0^1 M_{xy}^*(z) e^{-2\pi i n z} dz$$

$$Z_n = \int_0^1 M_z(z) e^{-2\pi i n z} dz$$

$$Q = \begin{bmatrix} F_0^+ & F_1^+ & \cdots & F_N^+ \\ F_0^+ * & F_1^- & \cdots & F_N^- \\ Z_0 & Z_1 & \cdots & Z_N \end{bmatrix}$$

The inverse Fourier transform to the state matrix Q gives the magnetization as

$$M_{xy}(z) = F_0^+ + \sum_{n=1}^{\infty} \left[F_n^+ e^{2\pi i n z} + (F_n^-)^* e^{-2\pi i n z}\right]$$

$$M_z(z) = Real\left\{Z_0 + 2\sum_{n=1}^{N} Z_n e^{2\pi i n z}\right\}$$

A.3 MORE DETAILS FOR EXPERIMENTS SETTINGS

We exploit the brain phantom of the BrainWeb Brain Database [10] to construct a set of realistic, high-resolution T1 maps and T2 maps as ground truth, which faithfully exhibit spatial distribution for different tissue compositions, including CSF, Grey matter, White matter, Adipose, Skin/muscle with corresponding T1, T2, and proton density values. The brain phantoms adopted in our experiment are the fuzzy version instead of the somewhat idealized crisp version, as the fuzzy version has taken into account partial volume effects that a voxel may contain a fragment of different tissue types, while the crisp version does not consider the inaccuracies associated with partial volume effects. The phantom data is obtained following the procedures: 1) obtain high-resolution real MRI images (weighted T1, weighted T2) from MRI machines using specific RF sequences, 2) apply classification algorithm to each voxel to distinguish the tissue type, including grey matter, white matter, skin, etc. 3) assign properties, such as T1, T2 values to each tissue type, which gives the high-resolution phantom data. In summary, T1 and T2 are identified phenomenologically to serve as gold standard reference.

In the experiment with different RF settings, we perform model training on one RF pulse sequence and evaluate the trained models on another different RF pulse sequence. Specifically, we adopted 3 different RF pulse sequences, including FISP [43], Spline5 [40], Spline11Noisy [40] with their flip angles shown in Figure 3a. The three RF pulse sequences have the same TR and TE settings, but different FA settings. Specifically, the FA of FISP is constituted a sinusoidal variation in the range of $0^\circ - 70^\circ$ degrees to ensure smoothly varying transient state of the magnetization [43]. The FA of Spline5 is spline-interpolated function with five control points randomly sampled from $0^\circ - 120^\circ$ degree, while the FA of SplineNoise11 is spline-interpolated function with 11 control points plus Gaussian random noise with 0 mean and 10 variance. Three FA settings are shown in Figure 3a. As suggested in [43], TE is chosen to be a constant of 10 ms across all the time points, TR is randomly time-varying sequence in the range of 11.5 - 14.5 ms with a Perlin noise pattern. FISP is used exclusively in the testing stage, while Spline5 and Spline11Noisy are used exclusively in the training stage. Under such settings, the performance of our BlochNet and other six models is compared in Table 2.

A.4 PHANTOM DATA IN DETAIL

A Physical phantom is an object created using physical materials that mimic the responses of human tissues under specific conditions. Since available real medical images are not enough to evaluate different image analysis procedures[10], phantom data contributes to comparing the performance of different medical imaging machines such as MRI [1]. However, the physical phantom with fixed shape and properties makes it hard to test medical imaging machines under various conditions. A digital phantom is a data file including any property of tissue that the imaging system is supposed to identify. Compared to the physical phantom, it can control factors that generate images such as slice thickness or contrast, leading to a dataset with a diverse distribution. For its generation, the best classifier selected by the neuroanatomist to assign each voxel of multiple MR images (e.g., T1 weighted or T2 weighted) to different tissue types such as white matter and grey matter. Then tissue parameters (T1, T2) are decided according to each tissue type for each voxel.

we select a few slices from each pair of T1/T2 phantom volume across 10 subjects (we select the fourth and fifth slices showing multiple tissues clearly). These slices are then vectorized as column vectors and stacked as a 2D matrix, leading to the ground truth tissue properties $\Theta \in \mathbb{R}^{N\times 2}$, where $N = 85,645$ denotes the total number of voxels from all slices. Here, we only consider the temporal information and ignore the spatial information, in other words, we treat every temporal sequence in different locations in each slice and subject as separate data points.

A.5 MORE RESULTS

A.5.1 GENERALIZATION ACROSS DIFFERENT DATA DISTRIBUTIONS

Figure 6 in appendix shows the predicted tissue properties (marked as red dots) using various models on anatomical MRF data, with the gold standard tissue properties marked as a blue line for reference. All four models perform well in the middle range of tissue properties and lead to small errors. However, the performance degrades to some extent at the head (small values) and tail (large values)

	Dictionary matching	FC	RNN	HYDRA	Autoencoder (FC-FC)	Autoencoder (RNN-RNN)	Causal (FC-Bloch)
Phantom data	6.6003	0.2609	0.2727	0.2363	0.2263	0.2784	**0.1024**
Anatomical data	6.0656	0.2773	0.3555	0.3884	0.2459	0.3353	**0.1344**

Table 3: Generalization performance across **different RF pulse sequences**: Spline5 in training, FISP in testing. All modes are trained on synthetic signatures with uniformly distributed T1 and T2 values as the label, and then tested on phantom data (top row) and anatomical data (bottom row). The mean square error between the ground truth and predicted tissue properties measures the generalization performance of these trained models on different RF settings, as well as different data distributions.

region. For example, Figure 6a, 6b, 6c tend to have a higher loss when T2 values are smaller than 30 ms. In comparison, our physics-based model demonstrates a more uniform stability on the prediction performance, and leads to small loss across the whole value range, especially when target T1, T2 values are close to the maximum and minimum, as shown in 6d.

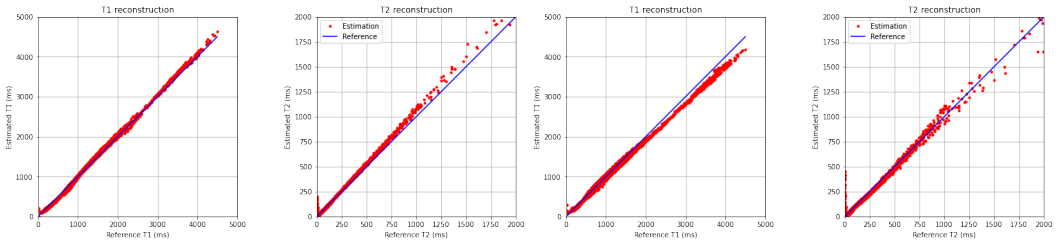

(a) FC. (b) HYDRA.

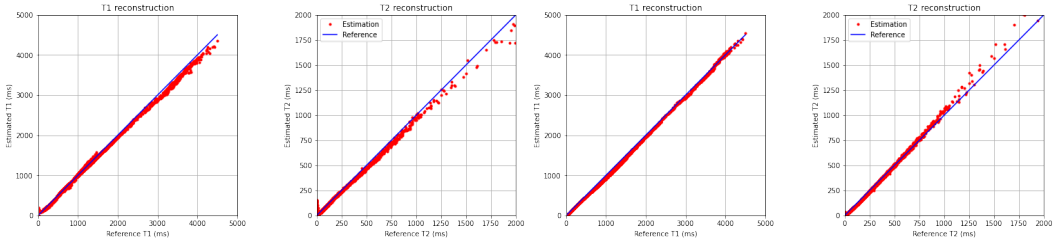

(c) Auto-encoder(FC-FC). (d) Physics(FC-Bloch).

Figure 6: Comparison of the generalization performance across **different data distributions** for 4 models. Training with synthetic data, and testing with anatomical data. Blue line: ground truth. Red dots: predicted values for tissue properties T1 and T2.

A.5.2 Generalization across different RF pulse sequences

Here, we additionally evaluate generalization performance across different RF pulse sequences where models are trained and tested with different types of RF pulse sequences. In the main paper, we use two flip angles sampled from two different distribution, Spline5 and SplineNoisy11, for generating training synthetic data. In comparison, we sampled two flip angles from one distribution, Spline5, for training stage and FISP flip angle is applied for test stage. Table 3 shows the same analysis as the Table 2 in the main paper. The proposed BlochNet shows the lowest reconstruction loss on both phantom and anatomical data, outperforming other comparison models.

A.6 More details about fast Bloch decoder based on efficient EPG

Since the released EPG code [59] has slow computation speed for solving numerical solutions, we adapt the EPG code [59] to achieve a much more efficient implementation, making it practical to use the exact MRI physics model as a decoder in the training procedure. A key change involves incorporating the torch jit package, and using batch-wise computation for the 3 Bloch stages includ-

ing RF pulse excitation, gradient-based slice selection, and relaxation, handling complex values in torch efficiently. This makes computation of the Bloch equations nearly a thousands times faster than the original EPG code. For example, generating a batch (1000) of magnetic responses of length 1000 takes only 1.6768 seconds in average using our EPG implementation, in comparison with 587.8097 seconds in average using the original EPG implementation [59] on the same CPU. Most of the benefit to faster computation comes from make it batch-wise computation using matrix multiplication. When the Bloch equation is applied as a decoder with an encoder with three layers of fully-connected model, our code takes about 0.1 hour in average for an epoch in training, while code [59] takes about 70 hours in average for an epoch on the same GPU(GTX 1080 Ti). Using torch jit gives such advantage for faster computation since it makes gradient computation process much efficient in end-to-end training procedure.

REFERENCES

[1] What are imaging phantoms. https://www.nist.gov/physics/what-are-imaging-phantoms.

[2] Jonas Adler and Ozan Öktem. Learned primal-dual reconstruction. *IEEE transactions on medical imaging*, 37(6):1322–1332, 2018.

[3] Bhairav Bipin Mehta, Simone Coppo, Debra Frances McGivney, Jesse Ian Hamilton, Yong Chen, Yun Jiang, Dan Ma, Nicole Seiberlich, Vikas Gulani, and Mark Alan Griswold. Magnetic resonance fingerprinting: a technical review. *Magnetic resonance in medicine*, 81(1): 25–46, 2019.

[4] Felix Bloch. Nuclear induction. *Physical review*, 70(7-8):460, 1946.

[5] Shengze Cai, Zhicheng Wang, Sifan Wang, Paris Perdikaris, and George Em Karniadakis. Physics-informed neural networks for heat transfer problems. *Journal of Heat Transfer*, 143 (6), 2021.

[6] Xiaozhi Cao, Congyu Liao, Zhixing Wang, Ying Chen, Huihui Ye, Hongjian He, and Jianhui Zhong. Robust sliding-window reconstruction for accelerating the acquisition of mr fingerprinting. *Magnetic resonance in medicine*, 78(4):1579–1588, 2017.

[7] Tsung-Han Chan, Kui Jia, Shenghua Gao, Jiwen Lu, Zinan Zeng, and Yi Ma. Pcanet: A simple deep learning baseline for image classification? *IEEE transactions on image processing*, 24 (12):5017–5032, 2015.

[8] Dongdong Chen, Mike E Davies, and Mohammad Golbabaee. Deep unrolling for magnetic resonance fingerprinting. In *2022 IEEE 19th International Symposium on Biomedical Imaging (ISBI)*, pp. 1–4. IEEE, 2022.

[9] Ouri Cohen, Bo Zhu, and Matthew S Rosen. MR fingerprinting deep reconstruction network (drone). *Magnetic resonance in medicine*, 80(3):885–894, 2018.

[10] D Louis Collins, Alex P Zijdenbos, Vasken Kollokian, John G Sled, Noor J Kabani, Colin J Holmes, and Alan C Evans. Design and construction of a realistic digital brain phantom. *IEEE transactions on medical imaging*, 17(3):463–468, 1998.

[11] Mike Davies, Gilles Puy, Pierre Vandergheynst, and Yves Wiaux. A compressed sensing framework for magnetic resonance fingerprinting. *SIAM Journal on Imaging Sciences*, 7(4): 2623–2656, 2014.

[12] Sean CL Deoni, Terry M Peters, and Brian K Rutt. High-resolution t1 and t2 mapping of the brain in a clinically acceptable time with despot1 and despot2. *Magnetic Resonance in Medicine: An Official Journal of the International Society for Magnetic Resonance in Medicine*, 53(1):237–241, 2005.

[13] Chao Dong, Chen Change Loy, Kaiming He, and Xiaoou Tang. Image super-resolution using deep convolutional networks. *IEEE Trans. Pattern Anal. Mach. Intell.*, 38(2):295–307, 2016.

[14] N Benjamin Erichson, Michael Muehlebach, and Michael W Mahoney. Physics-informed autoencoders for lyapunov-stable fluid flow prediction. *arXiv preprint arXiv:1905.10866*, 2019.

[15] Zhenghan Fang, Yong Chen, Mingxia Liu, Lei Xiang, Qian Zhang, Qian Wang, Weili Lin, and Dinggang Shen. Deep learning for fast and spatially constrained tissue quantification from highly accelerated data in magnetic resonance fingerprinting. *IEEE transactions on medical imaging*, 38(10):2364–2374, 2019.

[16] Zhenghan Fang, Yong Chen, Dong Nie, Weili Lin, and Dinggang Shen. Rca-u-net: Residual channel attention u-net for fast tissue quantification in magnetic resonance fingerprinting. In *International Conference on Medical Image Computing and Computer-Assisted Intervention*, pp. 101–109. Springer, 2019.

[17] Jonas Gehring, Michael Auli, David Grangier, Denis Yarats, and Yann N Dauphin. Convolutional sequence to sequence learning. *arXiv preprint arXiv:1705.03122*, 2017.

[18] Mohammad Golbabaee, Guido Buonincontri, Carolin M Pirkl, Marion I Menzel, Bjoern H Menze, Mike Davies, and Pedro A Gómez. Compressive mri quantification using convex spatiotemporal priors and deep encoder-decoder networks. *Medical Image Analysis*, 69:101945, 2021.

[19] Ian Goodfellow, Yoshua Bengio, Aaron Courville, and Yoshua Bengio. *Deep learning*, volume 1. MIT press Cambridge, 2016.

[20] Jesse I Hamilton, Danielle Currey, Sanjay Rajagopalan, and Nicole Seiberlich. Deep learning reconstruction for cardiac magnetic resonance fingerprinting t1 and t2 mapping. *Magnetic Resonance in Medicine*, 85(4):2127–2135, 2021.

[21] Kaiming He, Xiangyu Zhang, Shaoqing Ren, and Jian Sun. Deep residual learning for image recognition. In *Proc. IEEE Conf. Comput. Vision Pattern Recog*, pp. 770–778, 2016.

[22] Kaiming He, Xiangyu Zhang, Shaoqing Ren, and Jian Sun. Identity mappings in deep residual networks. In *Proc. Eur. Conf. Comput. Vision*, pp. 630–645. Springer, 2016.

[23] Jurgen Hennig. Echoes – how to generate, recognize, use or avoid them in mr-imaging sequences. part i: Fundamental and not so fundamental properties of spin echoes. *Concepts in Magnetic Resonance*, 3(3):125–143, 1991.

[24] Geoffrey Hinton, Li Deng, Dong Yu, George E Dahl, Abdel-rahman Mohamed, Navdeep Jaitly, Andrew Senior, Vincent Vanhoucke, Patrick Nguyen, Tara N Sainath, et al. Deep neural networks for acoustic modeling in speech recognition: The shared views of four research groups. *IEEE Signal processing magazine*, 29(6):82–97, 2012.

[25] Elisabeth Hoppe, Gregor Körzdörfer, Tobias Würfl, Jens Wetzl, Felix Lugauer, Josef Pfeuffer, and Andreas Maier. Deep learning for magnetic resonance fingerprinting: A new approach for predicting quantitative parameter values from time series. *Stud Health Technol Inform*, 243: 202–206, 2017.

[26] Truong Son Hy, Shubhendu Trivedi, Horace Pan, Brandon M Anderson, and Risi Kondor. Predicting molecular properties with covariant compositional networks. *The Journal of chemical physics*, 148(24):241745, 2018.

[27] Kyong Hwan Jin, Michael T McCann, Emmanuel Froustey, and Michael Unser. Deep convolutional neural network for inverse problems in imaging. *IEEE Transactions on Image Processing*, 26(9):4509–4522, 2017.

[28] Beomgu Kang, Byungjai Kim, HyunWook Park, and Hye-Young Heo. Learning-based optimization of acquisition schedule for magnetization transfer contrast mr fingerprinting. *NMR in Biomedicine*, 35(5):e4662, 2022.

[29] George Em Karniadakis, Ioannis G Kevrekidis, Lu Lu, Paris Perdikaris, Sifan Wang, and Liu Yang. Physics-informed machine learning. *Nature Reviews Physics*, 3(6):422–440, 2021.

[30] Vera Catharina Keil, Stilyana Peteva Bakoeva, Alina Jurcoane, Mariya Doneva, Thomas Amthor, Peter Koken, Burkhard Mädler, Guido Lüchters, Wolfgang Block, Ullrich Wüllner, et al. A pilot study of magnetic resonance fingerprinting in parkinson's disease. *NMR in Biomedicine*, 33(11):e4389, 2020.

[31] Niki Kilbertus, Giambattista Parascandolo, and Bernhard Schölkopf. Generalization in anticausal learning. *arXiv preprint arXiv:1812.00524*, 2018.

[32] Jiwon Kim, Jung Kwon Lee, and Kyoung Mu Lee. Deeply-recursive convolutional network for image super-resolution. In *Proc. IEEE Conf. Comput. Vision Pattern Recog*, pp. 1637–1645, 2016.

[33] Sewon Kim, Hanbyol Jang, Seokjun Hong, Yeong Sang Hong, Won C Bae, Sungjun Kim, and Dosik Hwang. Fat-saturated image generation from multi-contrast mris using generative adversarial networks with bloch equation-based autoencoder regularization. *Medical Image Analysis*, 73:102198, 2021.

[34] Alex Krizhevsky, Ilya Sutskever, and Geoffrey E Hinton. Imagenet classification with deep convolutional neural networks. In *Advances in neural information processing systems*, pp. 1097–1105, 2012.

[35] Lei Le, Andrew Patterson, and Martha White. Supervised autoencoders: Improving generalization performance with unsupervised regularizers. *Advances in neural information processing systems*, 31, 2018.

[36] Yann LeCun, Yoshua Bengio, and Geoffrey Hinton. Deep learning. *Nature*, 521(7553):436, 2015.

[37] Philip K Lee, Lauren E Watkins, Timothy I Anderson, Guido Buonincontri, and Brian A Hargreaves. Flexible and efficient optimization of quantitative sequences using automatic differentiation of bloch simulations. *Magnetic resonance in medicine*, 82(4):1438–1451, 2019.

[38] Congyu Liao, Berkin Bilgic, Mary Kate Manhard, Bo Zhao, Xiaozhi Cao, Jianhui Zhong, Lawrence L Wald, and Kawin Setsompop. 3d mr fingerprinting with accelerated stack-of-spirals and hybrid sliding-window and grappa reconstruction. *Neuroimage*, 162:13–22, 2017.

[39] Gilad Liberman, Yoram Louzoun, and Dafna Ben Bashat. T1 mapping using variable flip angle spgr data with flip angle correction. *Journal of Magnetic Resonance Imaging*, 40(1):171–180, 2014.

[40] Hongyan Liu, Oscar van der Heide, Cornelis AT van den Berg, and Alessandro Sbrizzi. Fast and accurate modeling of transient-state, gradient-spoiled sequences by recurrent neural networks. *NMR in Biomedicine*, 34(7):e4527, 2021.

[41] Weiyang Liu, Zhen Liu, Liam Paull, Adrian Weller, and Bernhard Schölkopf. Structural causal 3d reconstruction. In *Proc. Eur. Conf. Comput. Vision*, 2022.

[42] Alexander Loktyushin, Kai Herz, Nam Dang, Felix Glang, Anagha Deshmane, Simon Weinmüller, Arnd Doerfler, Bernhard Schölkopf, Klaus Scheffler, and Moritz Zaiss. Mrzero-automated discovery of mri sequences using supervised learning. *Magnetic Resonance in Medicine*, 86(2):709–724, 2021.

[43] Dan Ma, Vikas Gulani, Nicole Seiberlich, Kecheng Liu, Jeffrey L Sunshine, Jeffrey L Duerk, and Mark A Griswold. Magnetic resonance fingerprinting. *Nature*, 495(7440):187, 2013.

[44] Zhiping Mao, Ameya D Jagtap, and George Em Karniadakis. Physics-informed neural networks for high-speed flows. *Computer Methods in Applied Mechanics and Engineering*, 360: 112789, 2020.

[45] Andreas Maurer, Massimiliano Pontil, and Bernardino Romera-Paredes. The benefit of multitask representation learning. *Journal of Machine Learning Research*, 17(81):1–32, 2016.

[46] Gal Mazor, Lior Weizman, Assaf Tal, and Yonina C Eldar. Low rank magnetic resonance fingerprinting. In *Engineering in Medicine and Biology Society (EMBC), 2016 IEEE 38th Annual International Conference of the*, pp. 439–442. IEEE, 2016.

[47] Gal Mazor, Lior Weizman, Assaf Tal, and Yonina C Eldar. Low-rank magnetic resonance fingerprinting. *Medical physics*, 45(9):4066–4084, 2018.

[48] George S Misyris, Andreas Venzke, and Spyros Chatzivasileiadis. Physics-informed neural networks for power systems. In *2020 IEEE Power & Energy Society General Meeting (PESGM)*, pp. 1–5. IEEE, 2020.

[49] Vishal Monga, Yuelong Li, and Yonina C Eldar. Algorithm unrolling: Interpretable, efficient deep learning for signal and image processing. *IEEE Signal Processing Magazine*, 38(2): 18–44, 2021.

[50] Ilkay Oksuz, Gastao Cruz, James Clough, Aurelien Bustin, Nicolo Fuin, Rene M Botnar, Claudia Prieto, Andrew P King, and Julia A Schnabel. Magnetic resonance fingerprinting using recurrent neural networks. In *2019 IEEE 16th International Symposium on Biomedical Imaging (ISBI 2019)*, pp. 1537–1540. IEEE, 2019.

[51] Maziar Raissi, Paris Perdikaris, and George E Karniadakis. Physics-informed neural networks: A deep learning framework for solving forward and inverse problems involving nonlinear partial differential equations. *Journal of Computational physics*, 378:686–707, 2019.

[52] Somnath Rakshit, Ke Wang, and Jonathan I Tamir. A gpu-accelerated extended phase graph algorithm for differentiable optimization and learning.

[53] Evan Scope Crafts, Hengfa Lu, Huihui Ye, Lawrence L Wald, and Bo Zhao. An efficient approach to optimal experimental design for magnetic resonance fingerprinting with b-splines. *Magnetic Resonance in Medicine*, 88(1):239–253, 2022.

[54] Nir Shlezinger, Jay Whang, Yonina C Eldar, and Alexandros G Dimakis. Model-based deep learning. *arXiv preprint arXiv:2012.08405*, 2020.

[55] Pingfan Song, Yonina C Eldar, Gal Mazor, and Miguel RD Rodrigues. Hydra: Hybrid deep magnetic resonance fingerprinting. *Medical physics*, 46(11):4951–4969, 2019.

[56] Pingfan Song, Herman Verinaz-Jadan, Carmel L Howe, Amanda J Foust, and Pier Luigi Dragotti. Light-field microscopy for the optical imaging of neuronal activity: When model-based methods meet data-driven approaches. *IEEE Signal Processing Magazine*, 39(2):58–72, 2022.

[57] Refik Soyak, Ebru Navruz, Eda Ozgu Ersoy, Gastao Cruz, Claudia Prieto, Andrew P King, Devrim Unay, and Ilkay Oksuz. Channel attention networks for robust mr fingerprint matching. *IEEE Transactions on Biomedical Engineering*, 69(4):1398–1405, 2021.

[58] Zhe Wang, Hongsheng Li, Qinwei Zhang, Jing Yuan, and Xiaogang Wang. Magnetic resonance fingerprinting with compressed sensing and distance metric learning. *Neurocomputing*, 174: 560–570, 2016.

[59] Matthias Weigel. Extended phase graphs: dephasing, rf pulses, and echoes-pure and simple. *Journal of Magnetic Resonance Imaging*, 41(2):266–295, 2015.

[60] Mingrui Yang, Yun Jiang, Dan Ma, Bhairav B Mehta, and Mark A Griswold. Game of learning bloch equation simulations for mr fingerprinting. *arXiv preprint arXiv:2004.02270*, 2020.

[61] Qinqin Yang, Yanhong Lin, Jiechao Wang, Jianfeng Bao, Xiaoyin Wang, Lingceng Ma, Zihan Zhou, Qizhi Yang, Shuhui Cai, Hongjian He, et al. Model-based synthetic data-driven learning (most-dl): Application in single-shot t2 mapping with severe head motion using overlapping-echo acquisition. *IEEE Transactions on Medical Imaging*, 2022.

[62] Yan Yang, Jian Sun, Huibin Li, and Zongben Xu. Admm-csnet: A deep learning approach for image compressive sensing. *IEEE transactions on pattern analysis and machine intelligence*, 42(3):521–538, 2018.